



# Prediction and measurement of incipient boiling heat flux in micro-channel heat sinks

Weilin Qu, Issam Mudawar \*

*Boiling and Two-phase Flow Laboratory, School of Mechanical Engineering, Purdue University, West Lafayette, IN 47907, USA*

Received 2 November 2001; received in revised form 6 March 2002

## Abstract

Experiments were performed to measure the incipient boiling heat flux in a heat sink containing 21 rectangular (231  $\mu\text{m}$  wide and 713  $\mu\text{m}$  deep) micro-channels. Tests were performed using deionized water with inlet liquid velocities of 0.13–1.44 m/s, inlet temperatures of 30, 60 and 90 °C, and an outlet pressure of 1.2 bar. Using a microscope, boiling incipience was identified when the first bubbles were detected growing at, and departing from the micro-channel wall near the outlet. A comprehensive model was developed to predict the incipient boiling heat flux, accounting for the complexities of bubble formation along the flat and corner regions of a rectangular flow channel, as well as the likelihood of bubbles growing sufficiently large to engulf the entire flow area of a micro-channel. The model is based on a bubble departure criterion, which combines both mechanical considerations (force balance on a bubble) and thermal considerations (superheating entire bubble interface). The model shows good agreement with the experimental results. © 2002 Elsevier Science Ltd. All rights reserved.

## 1. Introduction

Micro-channel cooling has emerged in recent years as a highly effective means for dissipating large amounts of heat from small areas. It has been proposed for cooling high power density devices such as microprocessors and laser diode arrays. A micro-channel heat sink typically contains a large number of parallel micro-channel coolant passages ranging in size from 10 to 1000  $\mu\text{m}$ . Liquids such as water and fluorochemicals are two types of coolant that are favored with micro-channel heat sinks. Micro-channel heat sinks are classified into single-phase or two-phase, depending on whether boiling occurs in the micro-channels.

Single-phase micro-channel heat sinks have been studied quite extensively during the last two decades [1–6]. Test results have demonstrated the technical merits of single-phase micro-channel heat sinks compared to macro cooling systems, namely, the ability to produce

very large heat transfer coefficients, small size and volume per heat load, and small coolant inventory requirements.

Two-phase micro-channel heat sinks offer those same attributes while providing the following important advantages over their single-phase counterparts:

- (1) Much higher convective heat transfer coefficients are possible once boiling commences inside the micro-channels.
- (2) Better temperature uniformity is achieved with a two-phase micro-channel heat sink. Given the small coolant flow rates used in micro-channel heat sinks, applying a high heat flux to a single-phase heat sink can result in an unusually large stream-wise temperature rise in both the cooling liquid and heat sink, which can be very detrimental to temperature sensitive devices. A two-phase heat sink relies upon latent, rather than sensible, heat exchange which helps maintain stream-wise temperature uniformity at a level set largely by the coolant's saturation temperature.
- (3) Two-phase micro-channel heat sinks require much smaller coolant flow rates than single-phase heat

\* Corresponding author. Tel.: +1-765-494-5705; fax: +1-765-494-0539.

E-mail address: [mudawar@ecn.purdue.edu](mailto:mudawar@ecn.purdue.edu) (I. Mudawar).



well as inlet and exit effects. The model predictions were in good agreement with the experimental results. CHF values in excess of  $200 \text{ W/cm}^2$  were possible with both heat sinks using miniscule flow rates. Peng and Wang [12] investigated the boiling characteristics of subcooled water through  $600 \times 700 \mu\text{m}^2$  micro-channels. Their results indicate that, once initiated, nucleate boiling quickly became fully developed. Jiang et al. [14] conducted visualization studies on boiling of water in triangular micro-channels with nominal widths of 50 and  $100 \mu\text{m}$ . At low heat fluxes, individual bubbles were observed growing and departing inside the micro-channels. Increasing the heat flux triggered an abrupt change in flow pattern to unstable slug flow. Further increases in heat flux culminated in stable annular flow. Interestingly, the bubbly flow regime, common to macro flow boiling systems, was never observed. Ravigururajan [15] studied boiling and two-phase flow of R-124 in heat sinks containing parallel and diamond-oriented rectangular  $1000 \times 270 \mu\text{m}^2$  micro-channels. The heat transfer coefficient decreased with increases in wall superheat and exit vapor quality. Kennedy et al. [16] studied incipient boiling and onset of flow instability (OFI) for subcooled water flow in uniformly heated micro-tubes with diameters of 1.17 and 1.45 mm. For the smaller channel, significant deviation was found between experimental results and prior incipient boiling correlations. Zhang et al. [17] studied boiling of water in rectangular micro-channels with hydraulic diameters from 25 to  $60 \mu\text{m}$  and aspect ratios from 1.0 to 3.5, and a nearly constant heat flux boundary. Nucleation and small bubble growth were observed inside the micro-channels. Higher heat fluxes resulted in annular two-phase flow.

The aforementioned studies provide valuable insight into several aspects of boiling and two-phase flow in micro-channels. However, the understanding of two-phase micro-channel flow remains elusive, considering

the lack of reliable predictive tools for practical heat sink design. Compounding this problem is the observation made by many of these investigators, that the flow patterns, correlations and models available for macro two-phase systems are unsuitable to micro-channel flows.

This study focuses on measuring and predicting the incipient boiling heat flux in a micro-channel heat sink. This phenomenon is particularly important in micro-channel flows for several reasons. First, the ability to predict this condition is of paramount importance both as an upper design limit for heat sinks that are intended for single-phase cooling only, and as a lower limit for two-phase heat sinks intended for maximum heat dissipation. Second, incipient boiling in micro-channels seems to mark an abrupt transition from liquid flow to two-phase slug flow, which is not commonly encountered in macro two-phase systems. Thirdly, understanding this phenomenon is an integral part of a micro-channel heat sink design methodology.

In this paper, a comprehensive model is developed to predict the incipient boiling heat flux. This model accounts for all the complexities of bubble formation along the flat and corner regions of a rectangular flow channel, including the likelihood of bubbles growing sufficiently large to engulf the entire flow area of a micro-channel. The model predictions are validated with experimental data for water covering a broad range of velocity and subcooling.

## 2. Experimental apparatus and procedure

### 2.1. Test facility

As shown in Fig. 1, deionized water was circulated from a reservoir in a closed flow loop that was configured to achieve precise pressure, temperature, and flow

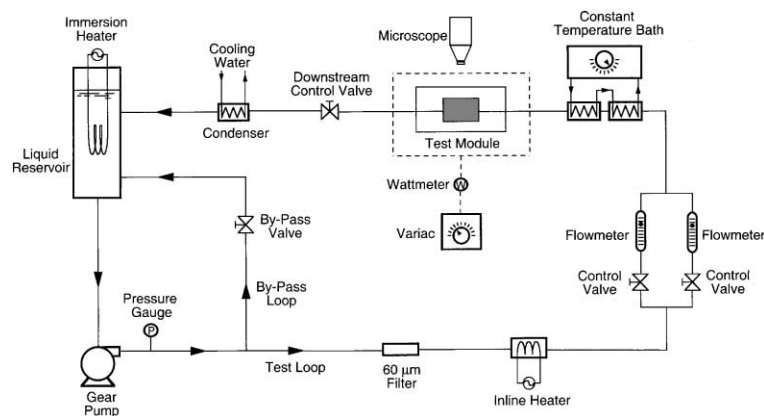


Fig. 1. Flow loop.

rate control at the test module. The water was circulated through the loop by a gear pump, and controlled by throttling valves located both upstream of the test module as well as in a bypass. The test module flow first passed through a filter to prevent any solid particles from blocking the micro-channels. The flow then entered an inline heater to modulate the water temperature close to the desired module inlet temperature. Exiting the inline heater, the water was routed into one of two rotameters for volume flow rate measurement. The flow then entered a heat exchanger, which was connected to a constant temperature bath, for fine temperature control just upstream of the test module. A throttling valve was installed downstream of the test module to control the water outlet pressure. A water-cooled condenser was situated downstream of this valve to condense any vapor exiting the test module before the water returned to the reservoir.

The test module consisted of a micro-channel heat sink, housing, cover plate, and 12 cartridge heaters as illustrated in Fig. 2. Fig. 3 shows a cross-sectional view of the assembled test module.

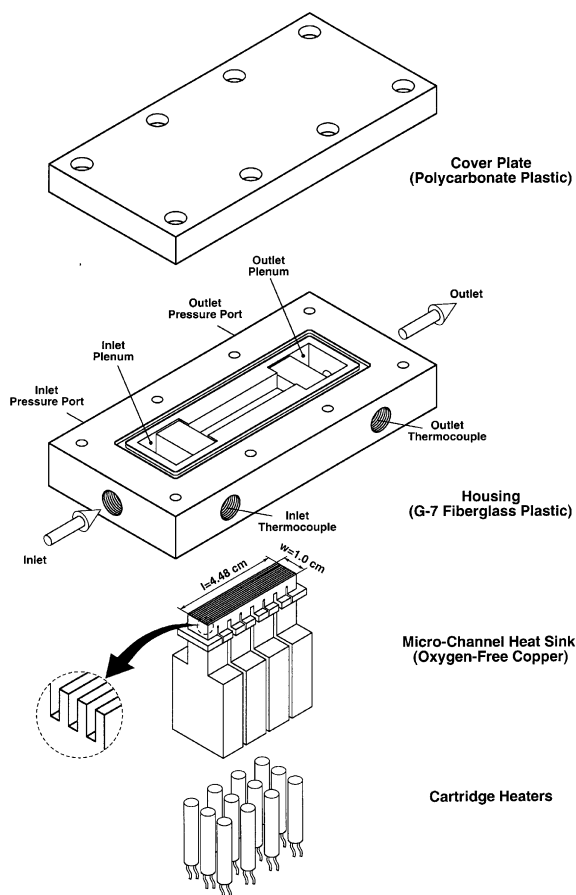


Fig. 2. Test module construction.

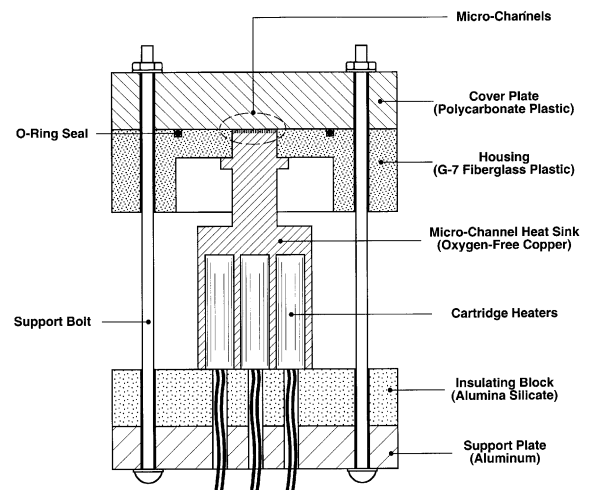


Fig. 3. Cross-section of test module assembly.

sink was fabricated from a single-block of oxygen-free copper. The planform (top) surface of the heat sink was 1.0 cm wide and 4.48 cm long. Using a precision sawing technique, 21 rectangular micro-slots, measuring 231  $\mu\text{m}$  wide and 712  $\mu\text{m}$  deep, were equidistantly machined within the 1-cm width of the heat sink. Four Type K (Chromel–Alumel) thermocouples were inserted below the heat sink top surface to measure the axial temperature distribution inside the heat sink. Twelve 6.35 mm diameter holes were drilled into the bottom surface of the heat sink to accommodate the cartridge heaters. These cartridge heaters were powered by a 0–110 VAC variac and their total power dissipation measured by a precision wattmeter.

The heat sink housing was made from high-temperature G-7 fiberglass plastic. The central part of the housing was removed where the heat sink was inserted. A small protruding platform machined around the periphery of the heat sink ensured the top surface of the heat sink was flush with the top surface of the housing as shown in Fig. 3. RTV silicone rubber was applied along the interface between the housing and the heat sink to prevent leakage. The housing contained plenums both upstream and downstream of the micro-channels to ensure even distribution of the flow between micro-channels as well as even exit mixing. Two absolute pressure transducers were connected to the inlet and outlet plenums via pressure taps to measure the inlet and outlet pressures, respectively. Also located in the inlet and outlet plenums were two Type-K thermocouples to measure the inlet and outlet temperatures of the water, respectively.

A cover plate made from transparent polycarbonate plastic (Lexan) was bolted atop the housing. The cover plate and micro-slots in the heat sink top surface formed

closed micro-channels as shown in Fig. 3. An O-ring in the housing maintained a leak-proof assembly. A microscope was situated above the cover plate to observe bubble formation inside the micro-channels as illustrated in Fig. 1.

## 2.2. Experimental procedure

The water was first deaerated using an immersion heater situated inside the reservoir. The water was brought to a vigorous boil for at least one hour to force any dissolved gases to escape to the ambient. The flow loop components were then adjusted to yield the desired micro-channel inlet temperature,  $T_{in}$ , outlet pressure,  $P_{out}$ , and coolant inlet velocity,  $u_{in}$ . The latter was determined from measured volume flow rate,  $\dot{V}$ .

$$u_{in} = \frac{\dot{V}}{NA_c}, \quad (1)$$

where  $N$  and  $A_c$  are the number of micro-channels and cross-sectional area of a single micro-channel, respectively. Table 1 gives the operating conditions of this study.

After the flow became stable, the heater power was set to a point well below the incipient boiling heat flux. The power was then increased in small increments while the flow loop components were constantly adjusted to maintain the desired micro-channel inlet and exit conditions. At each power level, the heat sink was allowed to reach steady-state conditions, following which the inlet pressure,  $P_{in}$ , outlet temperature,  $T_{out}$ , heat sink temperatures, and heater power,  $P_W$ , were all measured. The input heat flux,  $q''$ , was based on the top planform area,  $A_t = 1.0 \times 4.48 \text{ cm}^2$ , of the heat sink.

$$q'' = \frac{P_W}{A_t}. \quad (2)$$

The flow inside the micro-channels was visually monitored with the aid of the microscope. The bubbles first appeared near the exit of several micro-channels. The heat flux measured at this point was defined as the incipient boiling heat flux,  $q''_i$ . Each test was terminated 3–4 power increments beyond the incipient boiling condition.

Table 1  
Operating conditions of present study

Cooling liquid	Inlet temperature, $T_{in}$ (°C)	Inlet velocity, $u_{in}$ (m/s)	Outlet pressure, $P_{out}$ (bar)
Deionized water	30.0	0.13–1.19	1.2
	60.0	0.16–1.34	1.2
	90.0	0.17–1.44	1.2

## 2.3. Measurement uncertainty

Heat loss to the ambient was estimated to be less than 1% of the total power input, which was confirmed by excellent agreement between electrical power input and measured enthalpy change of water flow in single-phase tests previously performed by the authors [6] using the same experimental apparatus. Therefore, heat losses were assumed negligible, and the cartridge heater electrical power, measured by a 0.5% accuracy wattmeter, was used for all heat flux calculations. The rotameters were calibrated at the desired water temperature using the standard weighting method, and the accuracy was determined to be better than 4%. The pressure transducers were calibrated against a known standard and the uncertainty in the pressure measurements was less than 3.5%. Error associated with the thermocouple measurements was smaller than  $\pm 0.3$  °C.

## 3. Incipient boiling model

### 3.1. Bubble departure criterion

Boiling incipience in large channels has been studied extensively for several decades [18,19]. The onset of nucleate boiling (ONB) criterion was commonly employed to predict the boiling incipience in large channels. Classical ONB models are based on the assumption that a bubble will grow beyond the mouth of a cavity only if the surrounding liquid is sufficiently superheated to maintain mechanical equilibrium at the bubble interface. What has been commonly observed at incipient boiling for subcooled flow in large channels is small bubbles nucleate, grow and collapse while still attached to the wall, as a thin bubble layer forms along the channel wall [20].

Visual observation in the present study proved bubble behavior at incipient boiling in micro-channels is quite different from that in large channels. At incipient boiling, a small number of nucleation sites appeared simultaneously close to the exit of several (typically five to eight) micro-channels, with one or two sites per micro-channel. The majority of the first bubbles were observed on the channel bottom wall, though a few bubbles did appear on the sidewalls. After nucleation, bubbles first grew to detachment size before departing into the liquid flow. The detachment size was comparable to that of the micro-channel cross-section for lower velocities and decreased progressively with increasing velocity. The detached bubbles moved to the downstream plenum where they collapsed.

These visual observations prove that boiling incipience in the micro-channel heat sink was accompanied by both bubble growth and departure. This indicates that

the classical ONB criterion may not be adequate for describing incipience conditions in micro-channels.

Several mechanistic models for bubble detachment can be found in the literature [21–25]. All these models are based on two key assumptions: (1) bubble departure will occur when the forces tending to detach the bubble overcome those which hold it onto the wall, and (2) a bubble can only grow and detach if the liquid near the bubble tip (lowest temperature point along the bubble interface) is at least equal to the saturation temperature.

The same hypotheses are adopted in the present model development. It is obvious that boiling incipience is a local phenomenon, which strongly depends on both the hydrodynamic and thermal conditions at the micro-channel exit. This dependence, especially with a bubble size sometimes comparable to that of the micro-channel, necessitates a detailed understanding of the velocity and temperature distributions in the liquid at the micro-channel exit. To facilitate this analysis, a two-dimensional unit cell containing a single micro-channel and surrounding solid is examined. Symmetry allows the results to be easily extended to the entire heat sink. Fig. 4 illustrates the unit cell, the corresponding coordinate system, and key notations. Dimensions of the unit cell are given in Table 2.

3.2. Mechanical considerations

3.2.1. Force balance on bubbles

In this study, the postulations about bubble shape and forces of Al-Hayes and Winterton [23] are adopted

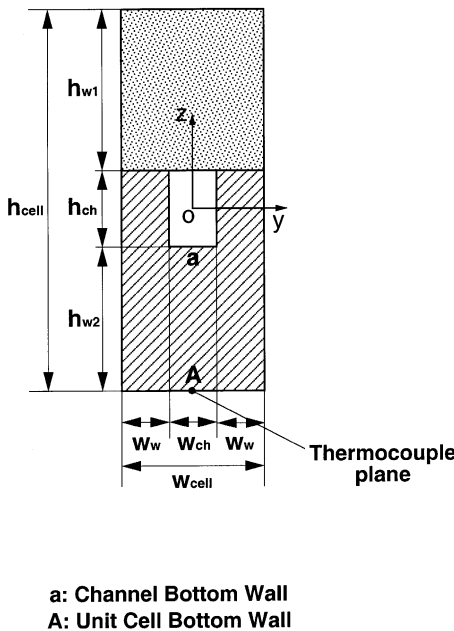


Fig. 4. Two-dimensional heat sink unit cell.

Table 2  
 Dimensions of unit cell

$w_w$ ( $\mu\text{m}$ )	$w_{ch}$ ( $\mu\text{m}$ )	$h_{w1}$ ( $\mu\text{m}$ )	$h_{ch}$ ( $\mu\text{m}$ )	$h_{w2}$ ( $\mu\text{m}$ )
118	231	12,700	713	2464

and modified to account for the complexities of bubble growth in a rectangular micro-channel, including bubble growth to a size comparable to that of the micro-channel, and bubble growth at or near the micro-channel corners. Given the rectangular shape of the micro-channel, vapor bubbles can be grouped into bottom wall bubbles, sidewall bubbles, and corner bubbles. The bubbles are treated as truncated spheres with contact angles at the wall equal to the equilibrium contact angle  $\theta_0$  as illustrated in Fig. 5(a). A corner bubble can be formed if the nucleate site is located exactly at the channel corner, or if a site is in the vicinity of a corner, and the bubble touches the neighboring wall during its growth.

It is commonly postulated that a bubble is subject to three forces: buoyancy force, drag force and surface tension force. The buoyancy force is neglected in the present analysis due to the horizontal flow orientation.

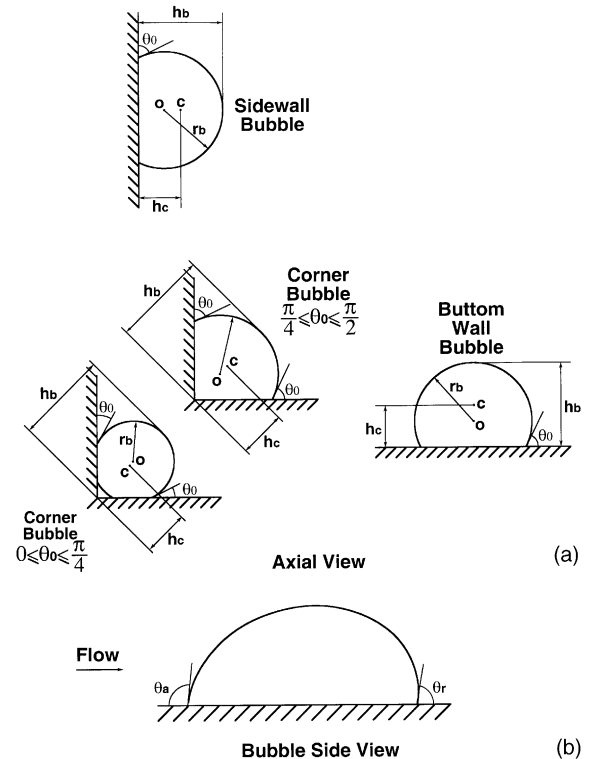


Fig. 5. (a) Appearance of departing bubbles along micro-channel cross-section, and (b) steamwise deformation of a bubble.

The drag force,  $F_d$ , is proportional to the dynamic pressure of the liquid and projected area of the bubble facing the flow [23].

$$F_d = C_d \frac{1}{2} \rho_l u_c^2 A_p, \tag{3}$$

where  $C_d$  is the drag coefficient,  $A_p$  is the projected area of the bubble, and  $u_c$  is the velocity at a point  $c$  half-way from the nucleation site to the bubble tip, as shown in Fig. 5(a).

$$h_c = \frac{h_b}{2}. \tag{4}$$

For bottom wall and sidewall bubbles,

$$A_p = r_b^2 (\pi - \theta_0 + \cos \theta_0 \sin \theta_0), \tag{5}$$

and for corner bubbles,

$$A_p = r_b^2 (\pi - 2\theta_0 + 2 \cos \theta_0 \sin \theta_0) \quad \text{for } 0 \leq \theta_0 \leq \frac{\pi}{4}, \tag{6a}$$

and

$$A_p = r_b^2 \left[ \frac{3\pi}{4} - \theta_0 + \cos \theta_0 (\cos \theta_0 + \sin \theta_0) \right] \quad \text{for } \frac{\pi}{4} \leq \theta_0 \leq \frac{\pi}{2}. \tag{6b}$$

The drag coefficient  $C_d$  can be calculated from [23]

$$C_d = \frac{24}{Re_b} \quad \text{for } 4 < Re_b < 20, \tag{7a}$$

and

$$C_d = 1.22 \quad \text{for } 20 < Re_b < 400, \tag{7b}$$

where  $Re_b$  is the bubble Reynolds number defined as

$$Re_b = \frac{\rho_l u_c (2r_b)}{\mu_l}. \tag{8}$$

According to Al-Hayes and Winterton [23], the surface tension force is a result of contact angle variations along the contact line due to the influence of the liquid flow. In this study, the surface tension force acting on the bubble is evaluated as

$$F_s = C_s \frac{1}{4} \sigma P_c (\cos \theta_r - \cos \theta_a), \tag{9}$$

where  $P_c$ ,  $\theta_r$  and  $\theta_a$  are the length of the contact line, receding contact angle and advancing contact angle, respectively. For bottom wall and sidewall bubbles,

$$P_c = 2\pi r_b \sin \theta_0, \tag{10}$$

and for corner bubbles,

$$P_c = 4\pi r_b \sin \theta_0 \quad \text{for } 0 \leq \theta_0 \leq \frac{\pi}{4}, \tag{11a}$$

and

$$P_c = 4r_b \sin \theta_0 \left[ \pi - \arccos \left( \frac{\cos \theta_0}{\sin \theta_0} \right) \right] \quad \text{for } \frac{\pi}{4} \leq \theta_0 \leq \frac{\pi}{2}. \tag{11b}$$

$\theta_a$  and  $\theta_r$  are modified contact angles at the bubble upstream and downstream stagnation points, respectively, as illustrated in Fig. 5(b), which can be calculated from the following correlations proposed by Winterton [24] for water:

$$\theta_a = \theta_0 + 10^\circ, \tag{12a}$$

and

$$\theta_r = \theta_0 - 10^\circ. \tag{12b}$$

$C_s$  in Eq. (9) is an empirical coefficient given by [23]

$$C_s = \frac{58}{\theta_0 + 5} + 0.14, \tag{13}$$

where  $\theta_0$  is in degrees.

### 3.2.2. Velocity field

As indicated earlier, the detailed velocity distribution at the micro-channel exit is required to evaluate the drag force according to Eq. (3). Fully developed single-phase liquid flow is assumed just upstream of the bubble, neglecting any disturbances introduced by the bubble generation. The velocity field can be determined from the analytical solution for fully developed laminar flow in a rectangular duct [26].

$$u = u_{out} \left\{ \frac{48}{\pi^3} \frac{\sum_{n=1,3,\dots}^{\infty} \frac{1}{n^3} (-1)^{(n-1)/2} \left[ 1 - \frac{\cosh \left( \frac{n\pi|y|}{h_{ch}} \right)}{\cosh \left( \frac{n\pi w_{ch}}{2h_{ch}} \right)} \right] \cos \left( \frac{n\pi|z|}{h_{ch}} \right)}{1 - \frac{192}{\pi^5} \left( \frac{h_{ch}}{w_{ch}} \right) \sum_{n=1,3,\dots}^{\infty} \frac{1}{n^5} \tanh \left( \frac{n\pi w_{ch}}{2h_{ch}} \right)} \right\}, \quad \text{for } -\frac{w_{ch}}{2} \leq y \leq \frac{w_{ch}}{2} \quad \text{and} \quad -\frac{h_{ch}}{2} \leq z \leq \frac{h_{ch}}{2}, \tag{14}$$

where  $u_{out}$  is the mean velocity at the micro-channel exit,

$$u_{out} = \frac{1}{A_c} \int_{A_c} u dA_c \tag{15}$$

A dimensionless velocity,  $U$ , is defined as the ratio of local velocity  $u$  to the mean exit velocity,  $u_{out}$ .

$$U = \frac{u}{u_{out}} \tag{16}$$

It is evident from Eq. (14) that the dimensionless velocity,  $U$ , depends solely on spatial variables. A contour map for  $U$  along the micro-channel cross-section is shown in Fig. 6.

3.2.3. Departing bubble size

The drag force and surface tension force are assumed to be in balance at the point of bubble departure.

$$F_d = F_s \tag{17}$$

Substituting Eqs. (3) and (9) into Eq. (17) and rearranging terms yields for bottom wall and sidewall bubbles

$$u_c^2 r_b = \frac{C_s}{C_d} \frac{\sigma}{\rho_f} \frac{\pi \sin \theta_0 (\cos \theta_r - \cos \theta_a)}{\pi - \theta_0 + \cos \theta_0 \sin \theta_0} \tag{18}$$

and for corner bubbles,

$$u_c^2 r_b = \frac{C_s}{C_d} \frac{\sigma}{\rho_f} \frac{2\pi \sin \theta_0 (\cos \theta_r - \cos \theta_a)}{\pi - 2\theta_0 + 2 \cos \theta_0 \sin \theta_0} \quad \text{for } 0 \leq \theta_0 \leq \frac{\pi}{4} \tag{19a}$$

and

$$u_c^2 r_b = \frac{C_s}{C_d} \frac{\sigma}{\rho_f} \frac{2 \left[ \pi - \arccos \left( \frac{\cos \theta_0}{\sin \theta_0} \right) \right] \sin \theta_0 (\cos \theta_r - \cos \theta_a)}{(3\pi/4) - \theta_0 + \cos \theta_0 (\cos \theta_0 + \sin \theta_0)} \tag{19b}$$

for  $\frac{\pi}{4} \leq \theta_0 \leq \frac{\pi}{2}$ .

Given the velocity field, nucleation site position, and all relevant material properties, the radius of a departing bubble,  $r_b$ , can be calculated by solving Eqs. (18), (19a) or (19b). It should be noted that  $u_c$  is also a function of  $r_b$  due to the dependence of point  $c$  on bubble geometry, which makes these equations too complex to be solved analytically. A numerical code was therefore developed to solve these equations. Fig. 7 illustrates the variation of  $r_b$  for bubbles at the bottom wall center, the sidewall center, and the channel corner, as a function of exit mean velocity  $u_{out}$ . Two equilibrium contact angle values,  $30^\circ$  and  $80^\circ$ , are used. It is expected that the actual equilibrium contact angle for water on a copper surface would be in between those two values. Once  $r_b$  is known, the geometry of the bubble can be easily specified.

3.2.4. Minimum velocity criterion

Fig. 7 shows the bubble size increases with decreasing  $u_{out}$ . There exists a minimum  $u_{out}$  for each bubble location, below which the bubble will grow beyond the confines of the micro-channel, and the bubble shape can no longer be treated as a truncated sphere. This condition defines a lower velocity limit,  $u_{out, min}$ , below which the present model will no longer be feasible. Although only one or two sites are activated within a micro-channel, the location of the site along the micro-channel wall is not readily known. To account for all possible

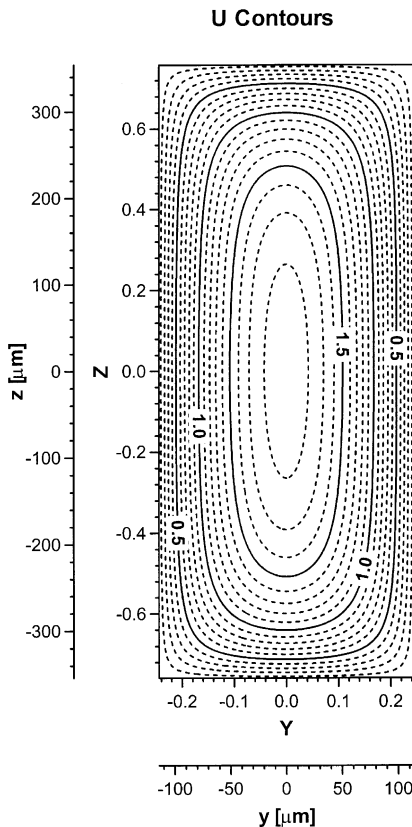


Fig. 6. Dimensionless liquid velocity contours at micro-channel exit.

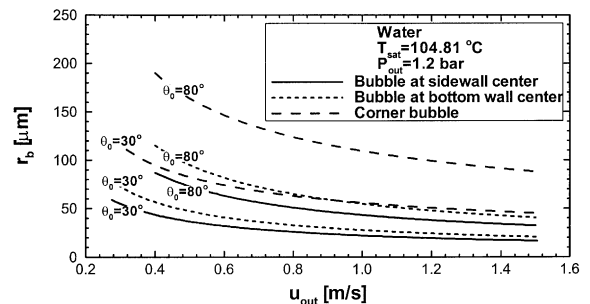


Fig. 7. Variation of bubble departure radius with mean liquid exit velocity for  $\theta_0 = 30^\circ$  and  $80^\circ$ .

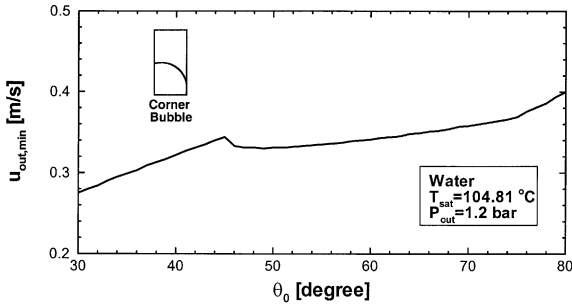


Fig. 8. Variation of  $u_{out, min}$  with equilibrium contact angle.

nucleation sites, the minimum velocity corresponding to every possible departing bubble along the wall was calculated and the highest value chosen as the  $u_{out, min}$  criterion for the micro-channel. This was done by selecting a large number of nucleation sites spaced equidistantly along the micro-channel wall, and conducting the minimum velocity calculations for each site. This analysis revealed  $u_{out, min}$  is always equal to the minimum  $u_{out}$  corresponding to the corner bubble, since this bubble is the first to fill the micro-channel as  $u_{out}$  decreases. Fig. 8 shows  $u_{out, min}$  generally increases with increasing  $\theta_0$ . However, a local maximum in  $u_{out, min}$  can be found along the curve, which corresponds to the transitional point of  $\theta_0 = 45^\circ$ . The reason for this transition is that the corner will be engulfed by the bubble once  $\theta_0$  exceeds  $45^\circ$ , as illustrated in Fig. 5(a).

### 3.3. Thermal considerations

#### 3.3.1. Temperature field

The temperature field at the micro-channel exit can be determined by solving a two-dimensional conjugate heat transfer domain which includes conduction in the solid region and convection to the liquid. Assuming fully developed single-phase laminar flow, the energy equations corresponding to the different regions of the heat sink unit cell, Fig. 4, can be written as follows:

$$k_f \left( \frac{\partial^2 T}{\partial y^2} + \frac{\partial^2 T}{\partial z^2} \right) = \frac{q'' w_{cell}}{A_c} \left( \frac{u}{u_{out}} \right) \quad \text{for the liquid region,} \quad (20)$$

$$k_s \left( \frac{\partial^2 T}{\partial y^2} + \frac{\partial^2 T}{\partial z^2} \right) = 0 \quad \text{for the copper heat sink,} \quad (21)$$

and

$$k_1 \left( \frac{\partial^2 T}{\partial y^2} + \frac{\partial^2 T}{\partial z^2} \right) = 0 \quad \text{for the Lexan cover plate.} \quad (22)$$

The boundary conditions applied to the unit cell are constant heat flux,  $q''$ , at the bottom boundary (wall A), and adiabatic conditions along all other boundaries.

Rather than directly solving Eqs. (20)–(22), a more universal approach [27,28] is adopted in the present model. First, the following dimensionless parameters are introduced:

$$Y = \frac{y}{w_{cell}}, \quad Z = \frac{z}{w_{cell}}, \quad \bar{T} = \frac{k_s(T - T_{out})}{q'' w_{cell}}, \quad (23)$$

$$U = \frac{u}{u_{out}},$$

where  $T_{out}$  is the mean exit temperature,

$$T_{out} = \frac{1}{u_{out} A_c} \int_{A_c} u T dA_c. \quad (24)$$

Eqs. (20)–(22) together with the boundary conditions can now be nondimensionalized as

$$\frac{k_f}{k_s} \left( \frac{\partial^2 \bar{T}}{\partial Y^2} + \frac{\partial^2 \bar{T}}{\partial Z^2} \right) = \frac{w_{cell}^2}{A_c} U \quad \text{for the liquid region,} \quad (25)$$

$$\frac{\partial^2 \bar{T}}{\partial Y^2} + \frac{\partial^2 \bar{T}}{\partial Z^2} = 0 \quad \text{for the copper heat sink,} \quad (26)$$

and

$$\frac{k_1}{k_s} \left( \frac{\partial^2 \bar{T}}{\partial Y^2} + \frac{\partial^2 \bar{T}}{\partial Z^2} \right) = 0 \quad \text{for the Lexan cover plate,} \quad (27)$$

with the boundary conditions,

$$\begin{aligned} \frac{\partial \bar{T}}{\partial Y} &= 0 \quad \text{at } Y = -W_w - \frac{W_{ch}}{2} \quad \text{and } Y = W_w + \frac{W_{ch}}{2}, \\ \frac{\partial \bar{T}}{\partial Z} &= 0 \quad \text{at } Z = H_{w1} + \frac{H_{ch}}{2}, \quad \text{and} \\ -\frac{\partial \bar{T}}{\partial Z} &= 1 \quad \text{at } Z = -H_{w2} - \frac{H_{ch}}{2}, \end{aligned} \quad (28)$$

where all the micro-channel dimensions are nondimensionalized with respect to  $w_{cell}$ .

A numerical scheme utilizing the finite difference method was developed to solve Eqs. (25)–(27) subject to the boundary conditions in Eq. (28) to determine the dimensionless temperature field. A detailed description of the numerical techniques employed in this model are provided by Qu and Mudawar [6], Weisber et al. [27] and Patankar [28,29]. Like the dimensionless velocity,  $U$ ,  $\bar{T}$  is also a function of spatial variables only. Fig. 9 shows the resulting dimensionless temperature field,  $\bar{T}$ , across the micro-channel cross-section.

#### 3.3.2. Superheating requirement and lowest bubble interface temperature

According to the second requirement for bubble detachment discussed earlier, a bubble should remain in a superheated liquid layer prior to departure. To meet this requirement, the lowest temperature along the departing bubble's interface should be larger than, or at least equal to the saturation temperature. In large channels, the

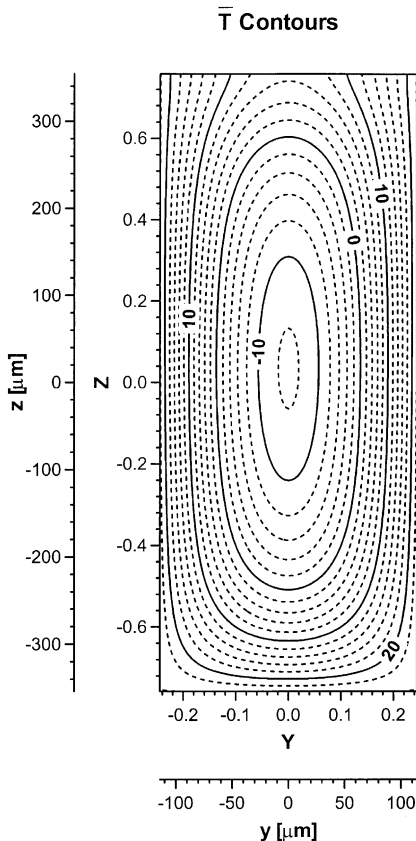


Fig. 9. Dimensionless liquid temperature contours at micro-channel exit.

bubble tip can be assumed the lowest temperature point along the bubble interface. However, this is not a valid assumption for bubbles in micro-channels, especially for bubbles near but not exactly at the corners. The temperature distribution around the bubble interface is therefore required in order to identify the lowest temperature point along the bubble interface. This can be accomplished once both the geometry of the departing bubble and the temperature field are determined.

### 3.4. Procedure for predicting incipient boiling heat flux

Based on the above analysis, the procedure to predicting the incipient boiling heat flux,  $q''_i$ , in the micro-channel heat sink can be summarized as follow:

- (1)  $u_{out}$  is set to be equal to the inlet velocity  $u_{in}$  in the present study due to the small liquid density variations between the inlet and exit.  $u_{out}$  is then compared to  $u_{out, min}$ , since the present model is not valid where  $u_{out}$  is smaller than  $u_{out, min}$ .
- (2) The velocity field at the micro-channel exit is determined using Eq. (14).

- (3) The bubble departure radius,  $r_b$ , is determined for a large number of nucleate sites equidistantly spaced along the micro-channel wall by solving Eqs. (18), (19a) or (19b).
- (4) The dimensionless temperature field,  $\bar{T}$ , is determined across the heat sink unit cell.
- (5) A small value is assigned to  $q''$ , and the mean exit temperature,  $T_{out}$ , is determined from the simple energy balance

$$\rho_l c_{p,l} u_{in} N A_c (T_{out} - T_{in}) = q'' A_t. \quad (29)$$

The liquid temperature,  $T$ , field is then determined by substituting  $q''$  and  $T_{out}$  into the dimensionless temperature,  $\bar{T}$ , field.

- (6) The lowest temperature along the bubble interface is calculated for each nucleation site along the micro-channel wall.
- (7) The value of heat flux,  $q''$ , is increased and steps (5) and (6) repeated until a bubble satisfies the superheat criterion, with the lowest temperature along its interface just exceeding the saturation temperature. The  $q''$  value at this condition is postulated to be the incipient boiling heat flux,  $q''_i$ , for the micro-channel heat sink.

### 3.5. Model predictions

The first bubble to satisfy the superheat criterion was determined to be a bottom wall bubble (hottest wall of micro-channel), which was located close to the channel corner. Interestingly, this bubble satisfies the superheat before the corner bubble does. This can be explained by the dimensionless temperature contour map shown in Fig. 9. This map shows the highest temperature is encountered at the channel corner where the temperature gradient is smallest due to weak heat transfer. This means a bubble near the corner region is much easier to nucleate than bubbles elsewhere along the micro-channel walls. The reason the corner bubble does not nucleate first is because its large radius (see Fig. 7) will cause it to penetrate deeper into the cooler liquid than a smaller bubble nucleating at the bottom wall close to the corner. This model prediction agrees well with visual observations as the majority of the first bubbles appeared on the channel bottom wall.

Fig. 10 shows the measured incipient boiling heat flux,  $q''_i$ , increases with increasing inlet velocity,  $u_{in}$ , and decreasing inlet temperature,  $T_{in}$ . Fig. 10 also displays greater sensitivity in the variation of  $q''_i$  with  $u_{in}$  for lower inlet temperatures. Also shown in Fig. 10 are the predictions based on the present model. Two different equilibrium contact angles are assumed,  $30^\circ$  and  $80^\circ$ , since the actual contact angle should be within this range for water on a copper surface. Fortunately, the differences between predictions using the two contact angles

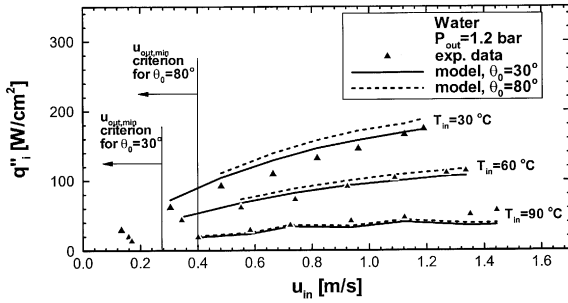


Fig. 10. Comparison of incipient boiling heat flux data and model predictions.

are not significant, and good agreement is shown between the predictions for both angles and the incipient boiling heat flux data. The  $u_{out, min}$  criteria corresponding to the two contact angles are also indicated in Fig. 10. The incipient boiling heat flux predictions are only valid for  $u_{in} > u_{out, min}$ .

This variation of  $q''_i$  with  $T_{in}$  and  $u_{in}$  can be partially explained by combining Eqs. (23) and (29), considering the lowest temperature point along the interface of the first bubble to depart as the reference point for  $\bar{T}$ , and setting  $T$  equal to  $T_{sat}$ .

$$q''_i = \frac{T_{sat} - T_{in}}{(\bar{T}w_{cell}/k_s) + (A_t/\rho_f c_{p,f} u_{in} NA_c)} \quad (30)$$

For a constant  $u_{in}$ ,  $\bar{T}$  is also constant since the geometry of the bubble depends solely on the flow velocity. Eq. (30) indicates  $q''_i$  will increase with decreasing  $T_{in}$ . On the other hand, holding  $T_{in}$  constant and increasing  $u_{in}$  will increase  $q''_i$ . However, increasing  $u_{in}$  can also cause an increase in  $\bar{T}$  due to the reduction in bubble radius, which yields the opposite trend in  $q''_i$ . Detailed calculations revealed the effect of increasing  $u_{in}$  is more dominant than the increase in  $\bar{T}$ , resulting in an overall increase in  $q''_i$ .

The heat sink outlet subcooling at incipient boiling is presented in Fig. 11 as a function of the inlet velocity,

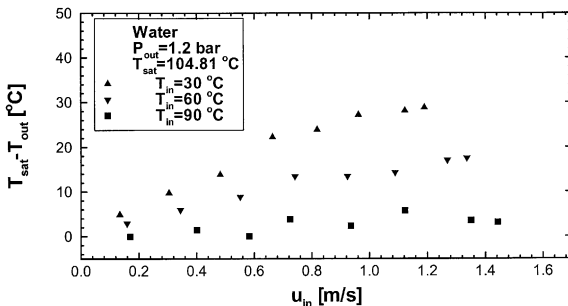


Fig. 11. Variation of measured outlet subcooling at boiling incipience with inlet velocity.

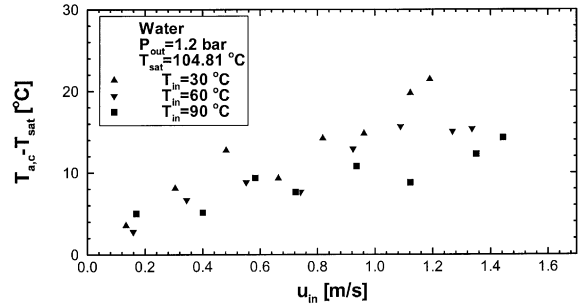


Fig. 12. Variation of incipient boiling superheat at center of bottom wall with inlet velocity.

$u_{in}$ . This outlet subcooling is the difference between the saturation temperature,  $T_{sat}$ , based on outlet pressure,  $P_{out}$ , and the measure outlet temperature,  $T_{out}$ . Fig. 11 shows the outlet subcooling increases with increasing inlet velocity,  $u_{in}$ , and decreasing inlet temperature  $T_{in}$ .

Unlike uniformly heated channels, where a single temperature can be used to represent the boiling incipience condition at the exit, the present micro-channel geometry involves appreciable temperature variations along the micro-channel wall. The superheat at the channel bottom wall (wall  $a$  in Fig. 4) center at the boiling incipience point is therefore used as a representative measure of incipient boiling temperatures for the micro-channel heat sink. This superheat is defined as the difference between the temperature at the center of the channel bottom wall,  $T_{a,c}$ , and the saturation temperature,  $T_{sat}$ .  $T_{a,c}$  was determined by substituting the measured  $q''_i$  and  $T_{out}$  into the calculated dimensionless temperature,  $\bar{T}$ , field. Like the incipient boiling heat flux trends in Fig. 10, Fig. 12 shows  $T_{a,c}$  increases with increasing inlet velocity,  $u_{in}$ , and decreasing inlet temperature,  $T_{in}$ .

#### 4. Conclusions

In this study, experiments were performed to measure the incipient heat flux in a micro-channel heat sink. The experimental work is complemented by the development of a new mechanistic model based on bubble departure criteria to predict the incipient boiling heat flux. Key findings from the study are as follows:

- (1) At incipient boiling, a small number of nucleation sites appear simultaneously close to the exit of several (typically five to eight) micro-channels, with one or two sites per micro-channel. Instead of collapsing locally, as they do in large channels, those first bubbles grow and depart into the liquid flow. Bubble departure size is comparable to that of the micro-channel for small velocities and decreases progressively with increasing velocity.

- (2) Both the incipient boiling heat flux and outlet subcooling increase with increasing inlet velocity and decreasing inlet temperature.
- (3) The channel bottom wall superheat at incipient boiling increases with increasing inlet velocity and decreasing inlet temperature. The measured superheat values (3–21 °C) prove no significant superheat is required to initiate boiling inside the micro-channel heat sink.
- (4) A mechanistic model was constructed to predict the incipient boiling heat flux. The model is based on a bubble departure criterion, which combines both mechanical considerations (force balance on a bubble) and thermal considerations (superheating entire bubble interface). This model is capable of predicting the size of bubbles departing from both the flat surfaces and corner regions, the temperature field around the bubble interface, and the location of the first bubble to depart. The model predictions show good agreement with the incipient boiling heat flux data.
- (5) The model points out many peculiarities of boiling incipience in micro-channels such as bubbles growing to the size of the micro-channel for low velocities (see Fig. 7). Another example of the unique nature of incipience in rectangular micro-channels is first bubble departure along the bottom wall near, but not at the hottest corners, because of the complex combined effect of bubble size and surrounding temperature field on the bubble departure.

### Acknowledgements

The authors are grateful for the support of the Office of Basic Energy Sciences of the US Department of Energy (Award no. DE-FG02-93ER14394 A7). The authors also thank Dr. Paul Zmola for his financial support of the hardware for this project.

### References

- [1] D.B. Tuckerman, R.F.W. Pease, High-performance heat sinking for VLSI, *IEEE Electron. Dev. Lett.* EDL-2 (1981) 126–129.
- [2] R.J. Phillips, Micro-channel heat sinks, in: A. Bar-Cohen, A.D. Kraus (Eds.) *Advances in Thermal Modeling of Electronic Components*, vol. 2, 1990, ASME Press, New York, pp. 109–184.
- [3] M.M. Rahman, F. Gui, Experimental measurements of fluid flow and heat transfer in microchannel cooling passages in a chip substrate, in: *Advances in Electronic Packaging*, ASME, New York, 1993, pp. 495–506.
- [4] K. Kawano, K. Minakami, H. Iwasaki, M. Ishizuka, Micro channel heat exchanger for cooling electrical equipment, in: R.A. Nelson Jr., L.W. Swanson, M.V.A. Bianchi, C. Camci (Eds.), *Proceedings of the ASME Heat Transfer Division*, ASME, Anaheim, CA, 1998, pp. 173–180 (HTD-Vol.361-3/PID-Vol.3).
- [5] T.M. Harms, M.J. Kazmierczak, F.M. Cerner, Developing convective heat transfer in deep rectangular microchannels, *Int. J. Heat Fluid Flow* 20 (1999) 149–157.
- [6] W. Qu, I. Mudawar, Experimental and numerical study of pressure drop and heat transfer in a single-phase micro-channel heat sink, *Int. J. Heat and Mass Transfer* 45 (2002) 2549–2565.
- [7] I. Mudawar, M.B. Bowers, Ultra-high critical heat flux (CHF) for subcooled water flow boiling—I. CHF data and parametric effects for small diameter tubes, *Int. J. Heat Mass Transfer* 42 (1999) 1405–1428.
- [8] D.D. Hall, I. Mudawar, Ultra-high critical heat flux (CHF) for subcooled water flow boiling—II. High-CHF database and design parameters, *Int. J. Heat Mass Transfer* 42 (1999) 1429–1456.
- [9] M.B. Bowers, I. Mudawar, High flux boiling in low flow rate, low pressure drop mini-channel and micro-channel heat sinks, *Int. J. Heat Mass Transfer* 37 (1994) 321–332.
- [10] M.B. Bowers, I. Mudawar, Two-phase electronic cooling using mini-channel and micro-channel heat sinks: part 1—design criteria and heat diffusion constraints, *J. Electron. Packaging* 116 (1994) 290–297.
- [11] M.B. Bowers, I. Mudawar, Two-phase electronic cooling using mini-channel and micro-channel heat sinks: part 2—flow rate and pressure drop constraints, *J. Electron. Packaging* 116 (1994) 298–305.
- [12] X.F. Peng, B.X. Wang, Forced convection and flow boiling heat transfer for liquid flowing through microchannels, *Int. J. Heat Mass Transfer* 36 (1993) 3421–3427.
- [13] X.F. Peng, H.Y. Hu, B.X. Wang, Boiling nucleation during liquid flow in microchannels, *Int. J. Heat Mass Transfer* 41 (1998) 101–106.
- [14] L. Jiang, M. Wong, Y. Zohar, Forced convection boiling in a microchannel heat sink, *J. Microelectromech. Syst.* 10 (2001) 80–87.
- [15] T.S. Ravigururajan, Impact of channel geometry on two-phase flow heat transfer characteristics of refrigerants in microchannel heat exchangers, *J. Heat Transfer* 120 (1998) 485–491.
- [16] J.E. Kennedy, G.M. Roach Jr., M.F. Dowling, S.I. Abdel-Khalik, S.M. Ghiaasiaan, S.M. Jeter, Z.H. Quershi, The onset of flow instability in uniformly heated horizontal microchannels, *J. Heat Transfer* 122 (2000) 118–125.
- [17] L. Zhang, J.M. Koo, L. Jiang, S.S. Banerjee, M. Ashegi, K.E. Goodson, J.G. Santiago, T.W. Kenny, Measurement and modeling of two-phase flow in microchannels with nearly-constant heat flux boundary conditions, in: A. Lee et al. (Eds.), *Micro-electro-mechanical Systems (MEMS) 2000*, MEMS-Vol.2, ASME, Orlando, FL, 2000, pp. 129–135.
- [18] T. Sato, H. Matsumura, On the conditions of incipient subcooled boiling and forced-convection, *Bull. JSME* 7 (1963) 392–398.
- [19] E.J. Davis, G.H. Anderson, The incipience of nucleate boiling in forced convection flow, *AIChE J.* 12 (1966) 774–780.

- [20] J.G. Collier, J.R. Thome, *Convective Boiling and Condensation*, third ed., Oxford University Press, Oxford, 1994.
- [21] S. Levy, Forced convection subcooled boiling—prediction of vapor volumetric fraction, *Int. J. Heat Mass Transfer* 10 (1967) 951–965.
- [22] F.W. Staub, The void fraction in subcooled boiling—prediction of the initial point of net vapor generation, *J. Heat Transfer* 90 (1968) 151–157.
- [23] R.A.M. Al-Hayes, R.H.S. Winterton, Bubble diameter in detachment in flowing liquids, *Int. J. Heat Mass Transfer* 24 (1981) 223–230.
- [24] R.H.S. Winterton, Flow boiling: prediction of bubble departure, *Int. J. Heat Mass Transfer* 27 (1984) 1422–1424.
- [25] J.T. Rogers, M. Salcudean, Z. Abdullah, D. Mcleod, D. Poirier, The onset of significant void in up-flow boiling of water at low pressure and velocities, *Int. J. Heat Mass Transfer* 30 (1987) 2247–2260.
- [26] R.K. Shah, A.L. London, *Laminar Flow Forced Convection in Ducts: A Source Book for Compact Heat Exchanger Analytical Data*, Academic press, New York, 1978, Supl. 1.
- [27] A. Weisberg, H.H. Bau, J.N. Zemel, Analysis of micro-channels for integrated cooling, *Int. J. Heat Mass Transfer* 35 (1992) 2465–2474.
- [28] S.V. Patankar, A numerical method for conduction in composite materials, flow in irregular geometries and conjugate heat transfer, in: *Proceedings of the sixth International Heat Transfer Conference*, vol. 3, Hemisphere, Toronto, Canada, 1978, pp. 297–302.
- [29] S.V. Patankar, *Numerical Heat Transfer and Fluid Flow*, Hemisphere, Washington, DC, 1980.